Proteasomes tether to two distinct sites at the nuclear pore complex

Sahradha Albert[a], Miroslava Schaffer[a], Florian Beck[a], Shyamal Mosalaganti[b], Shoh Asano[a,1], Henry F. Thomas[a], Jürgen M. Plitzko[a], Martin Beck[b], Wolfgang Baumeister[a,2], and Benjamin D. Engel[a,2]

[a]Department of Molecular Structural Biology, Max Planck Institute of Biochemistry, 82152 Martinsried, Germany; and [b]Structural and Computational Biology Unit, European Molecular Biology Laboratory, 69117 Heidelberg, Germany

Contributed by Wolfgang Baumeister, November 10, 2017 (sent for review October 12, 2017; reviewed by Eva Nogales and Alexander Varshavsky)

The partitioning of cellular components between the nucleus and cytoplasm is the defining feature of eukaryotic life. The nuclear pore complex (NPC) selectively gates the transport of macromolecules between these compartments, but it is unknown whether surveillance mechanisms exist to reinforce this function. By leveraging in situ cryo-electron tomography to image the native cellular environment of *Chlamydomonas reinhardtii*, we observed that nuclear 26S proteasomes crowd around NPCs. Through a combination of subtomogram averaging and nanometer-precision localization, we identified two classes of proteasomes tethered via their Rpn9 subunits to two specific NPC locations: binding sites on the NPC basket that reflect its eightfold symmetry and more abundant binding sites at the inner nuclear membrane that encircle the NPC. These basket-tethered and membrane-tethered proteasomes, which have similar substrate-processing state frequencies as proteasomes elsewhere in the cell, are ideally positioned to regulate transcription and perform quality control of both soluble and membrane proteins transiting the NPC.

proteasome | nuclear pore complex | quality control | focused ion beam | cryo-electron tomography

The 26S proteasome degrades polyubiquitinated proteins, a critical function for numerous cellular processes, including proteostasis and transcriptional control (1, 2). Proteasomes inhabit both the cytosol and nucleus and are enriched within the nuclei of many proliferating eukaryotic cells (3, 4). However, the specific functions of cytoplasmic and nuclear proteasomes are just beginning to emerge. Measurements of the relative proteasome activity in these two compartments vary greatly (5–7), with some models questioning whether nuclear proteasomes are proteolytically active or even fully assembled. These measurements are complicated by the use of indirect methods, which require the removal of proteasomes from cells to correlate proteasome function with the cellular compartment.

Nuclear proteasomes have been observed to localize to specific regions in different organisms and under changing physiological conditions (3, 8). In mammalian cells, proteasomes are often dispersed throughout the nucleoplasm but can also concentrate in nuclear foci, including PML bodies (9). In yeast, the protein Cut8/Sts1 tethers proteasomes to the nuclear envelope, likely by directly binding the inner nuclear membrane (INM) (10–12). However, the nuclear pore complex (NPC) may also participate in recruiting proteasomes to the nuclear envelope. In *Schizosaccharomyces pombe*, the localization of Cut8 and proteasomes to the nuclear envelope requires a TPR nucleoporin that forms the filaments of the NPC's nuclear basket (13). In *Saccharomyces cerevisiae*, immunoprecipitation experiments showed that the protein Esc1 can interact with both proteasomes and TPR nucleoporins (14). These studies raise the intriguing possibility that proteasomes may bind to the NPC basket. However, TPR nucleoporins also occupy regions of the nuclear envelope that are devoid of NPCs (13, 14), and it remains unknown whether proteasomes specifically localize to NPCs.

In situ cryo-electron tomography (cryo-ET) is ideally suited to investigate these questions of proteasome localization and activity, as it can assess the functional state and interaction partners of each proteasome by directly visualizing its macromolecular structure within the native cellular environment (15). We combined focused ion beam (FIB) milling of vitrified frozen cells (16–18) with cryo-ET to perform an extensive molecular-resolution structural survey of cytoplasmic and nuclear proteasomes within *Chlamydomonas reinhardtii*. This unicellular green alga provides highly organized organelle architecture and superb cryo-EM imaging properties, likely due to reduced molecular crowding, which enables reliable macromolecule identification and structure determination (19–22).

Results

After pruning our dataset based on tomogram reconstruction quality, our survey consisted of 76 tomograms of the nuclear envelope and its environs. Visual inspection of our tomograms revealed numerous 26S proteasomes throughout the nucleus and cytoplasm (Fig. 1*A*). Both side views (Fig. 1 *C* and *D*) and top views (Fig. 1*E*) of the proteasomes were readily identified, and fine structural features could be discerned by eye, such as the distinction between double-capped (Fig. 1*C*) and single-capped (Fig. 1*D*) proteasomes. To comprehensively identify all of the proteasomes in our tomograms, we searched the cellular volumes with a down-filtered template of a 20S core particle attached to one 19S cap, which has been

Significance

This study compares the native structures of cytosolic and nuclear proteasomes, visualized directly within cells. The assembly states and functional states of proteasomes in each compartment were similar, indicating comparable levels of proteolytic activity per proteasome. Nuclear proteasomes were tethered to two different sites at the nuclear pore complex (NPC): the inner nuclear membrane and the NPC basket. Structural analysis revealed mechanistic details of the two tethering interactions. These results present direct evidence that proteasomes bind at NPCs, establishing a cellular hub for protein degradation at the gateway between the nucleus and cytoplasm. This work demonstrates how cryo-electron tomography can reveal biological mechanisms by directly observing the interactions between molecular complexes within the native cellular environment.

Author contributions: J.M.P., W.B., and B.D.E. designed research; S. Albert, M.S., and B.D.E. performed research; S. Albert, F.B., S.M., S. Asano, H.F.T., M.B., and B.D.E. analyzed data; and S. Albert, W.B., and B.D.E. wrote the paper.

Reviewers: E.N., University of California, Berkeley; and A.V., California Institute of Technology.

The authors declare no conflict of interest.

Data deposition: Cryo-EM maps from subtomogram averaging, along with the tomogram shown in Fig. 1, were uploaded to the Electron Microscopy Data Bank, https://www.ebi.ac.uk/pdbe/emdb/ (accession nos. EMD-3932–EMD-3940 and EMD-3967).

[1]Present address: Internal Medicine Research Unit, Pfizer Inc., Cambridge, MA 02139.

[2]To whom correspondence may be addressed. Email: baumeist@biochem.mpg.de or engelben@biochem.mpg.de.

This article contains supporting information online at www.pnas.org/lookup/suppl/doi:10.1073/pnas.1716305114/-/DCSupplemental.

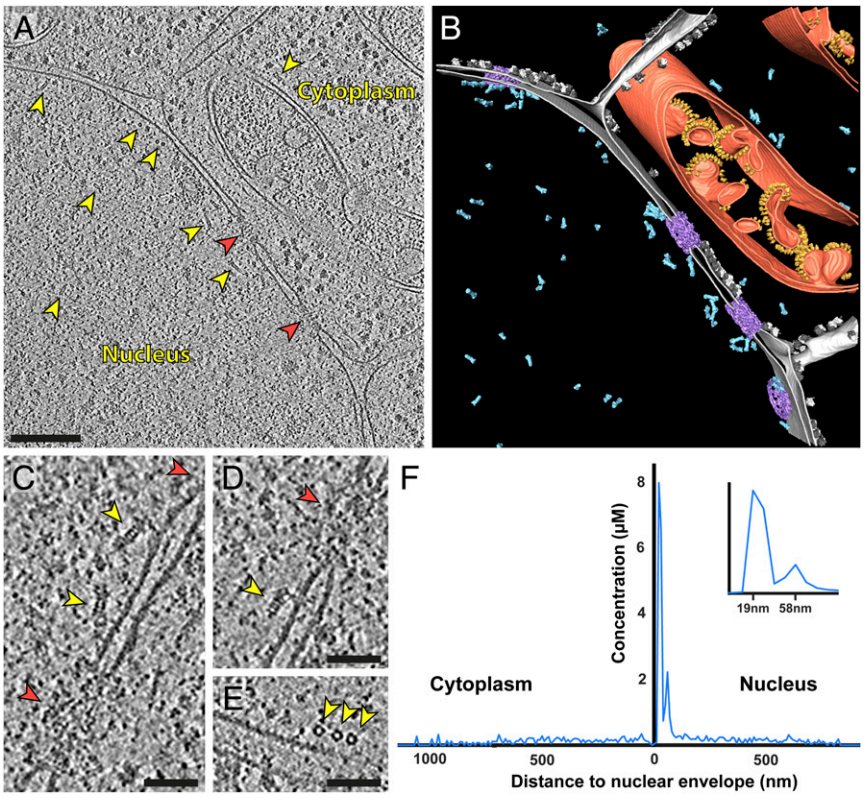

Fig. 1. Nuclear proteasomes cluster at the INM in *Chlamydomonas*. (*A*) Overview slice through a tomogram spanning the nucleus and cytoplasm (yellow arrows indicate proteasomes; red arrows indicate NPCs) and (*B*) corresponding segmentation, containing subtomogram averages of proteasomes (blue), NPCs (purple), ATP synthases (yellow), and ribosomes (white, 40S; dark gray, 60S), along with membranes of the nuclear envelope/ER (gray) and mitochondria (orange). (*C*–*E*) Close-up views of nuclear proteasomes at the INM: (*C*) double-capped side views, (*D*) single-capped side view, and (*E*) top views. (*F*) Proteasome concentration in concentric shells expanding from the two membranes of the nuclear envelope (zero point) into the cytoplasm (*Left*) and nucleus (*Right*). Values are summed from 61 tomograms. (*Inset*) Enlarged plot of the two distinct peaks of concentration near the INM. (Scale bars: 200 nm in *A*, 50 nm in *C*–*E*.)

shown to equally match both single-capped and double-capped proteasomes in situ (23). Subvolumes were extracted from the tomograms based on their cross-correlation scores, visually inspected to confirm the presence of a proteasome, and then subjected to subtomogram alignment and classification to produce a molecular-resolution average from 3,322 particles (Fig. S1). Using the refined positions and orientations from the aligned average, the proteasomes were mapped back into the cellular volumes with nanometer precision (Fig. 1*B*).

Positioning all of the proteasomes within the cellular environment led to a striking observation. While proteasomes were dispersed throughout the nucleus and cytoplasm, they also appeared to crowd at the INM in the vicinity of NPCs. To quantify this phenomenon throughout our dataset, we calculated the concentration of proteasomes within expanding shells extending from both sides of the nuclear envelope (Fig. 1*F*). The average concentrations of dispersed proteasomes in the cytoplasm and nucleoplasm were nearly identical, at 157 nM and 156 nM, respectively. This concentration is similar to previous cytoplasmic measurements from rat neurons (23) and yeast (4). However, directly adjacent to the INM, the local proteasome concentration dramatically increased. This massive accumulation was subdivided into two sharp peaks, one peak 58 nm from the membrane with a maximum concentration of 2.26 μM and a second peak 19 nm from the membrane with a maximum concentration of 8.11 μM. The accumulation of proteasomes at the INM is not limited to algae, as it has previously been observed in yeast and *Drosophila* S2 cells (10, 24, 25). Our observation in *Chlamydomonas* expands the documented prevalence of this phenomenon to another kingdom of eukaryotic life.

To investigate whether there is a structural basis for proteasome localization at the INM, we subjected the initial proteasome subtomogram average to several rounds of classification, sorting the subvolumes into structurally homogeneous classes (Fig. S2). The whole population was first separated into single-capped and double-capped assembly states (Fig. 2*A* and Fig. S3). These refined averages were then cut in half along the medial axis of the 20S core particle and pooled together to allow classification of each individual 19S cap (5,498 total particles). During its functional cycle, the 19S particle is known to undergo large-scale conformational changes that can be observed both in isolated proteasomes (26, 27) and in situ (23). Classification of our dataset yielded well-resolved structures for the S1 ground state, which is not engaged with substrate, and the S3 substrate-processing state (Fig. 2*B*). Interestingly, in addition to 19S functional states, classification also revealed distinct 19S binding states. The population was subdivided into "free" unbound caps, "basket-tethered" caps that were attached to an extra density (named for their association with the NPC nuclear basket, see below), and "membrane-tethered" caps that were bound to a membrane-like density via a thin connection (Fig. 2*C*).

To more clearly resolve the structures in the basket-tethered and membrane-tethered classes, we used a local mask to focus the subtomogram alignment on the site where the extra densities bind the proteasome (Fig. 2 *E* and *F*). Following refinement, the extra density in the basket-tethered class grew from a small globular density into an extended bifurcated structure (Fig. S4*A*), while the membrane-tethered density transformed into three smaller densities protruding from a smooth membrane surface, only one of which was attached to the proteasome (Fig. S4*B*). Based on its size, we roughly estimate the mass of the density that tethers proteasomes to the membrane to be 20–50 kDa. Rigid-body fitting of a high-resolution yeast S1 proteasome structure (26) into the refined averages revealed that the extra densities in both classes likely bind the proteasome at Rpn9. Rpn9 is a nonessential subunit of the proteasome that facilitates the incorporation of its neighbor, Rpn10, into 19S particles and promotes proteasome stability (28). However, unlike Rpn10, which has multiple protein interaction domains and binds polyubiquitin chains (29, 30), no well-characterized extraproteasomal interaction partners have been found for Rpn9. While it is possible that these two subunits cooperate in binding the extra densities, the tethering interaction does not appear to compete with the binding of polyubiquitin to Rpn10, as 19S structures in the basket-tethered and membrane-tethered classes show the same level of substrate processing as those in the free class (Fig. S5).

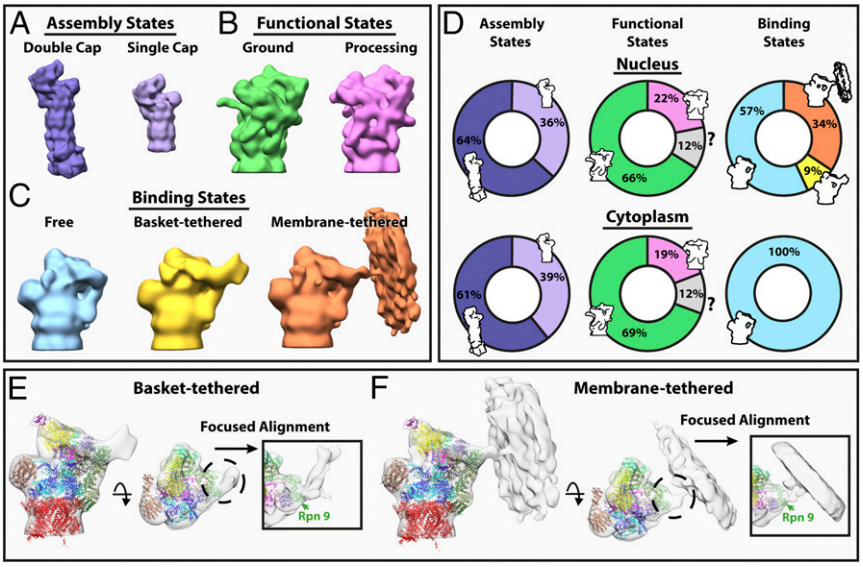

Fig. 2. Structural classification of the proteasome population. Subtomogram averages of (*A*) 26S assembly states: double-capped (purple, 21.9-Å resolution) and single-capped (lavender, 23.8-Å resolution); (*B*) 19S functional states: ground state (green, 17.2-Å resolution) and substrate-processing state (pink, 19.6-Å resolution); (*C*) 19S binding states: free (blue, 23.8-Å resolution), basket-tethered (yellow, 34.5-Å resolution), and membrane-tethered (orange, 24.9-Å resolution). In *B* and *C*, proteasomes were cut in half, and each cap was classified individually. (*D*) Population statistics of proteasome states within the nucleus (*Upper* row) and the cytoplasm (*Lower* row). "?" are unknown functional states that were not clearly classified. (*E* and *F*) Focused alignment of the extra densities bound to the proteasome in the (*E*) basket-tethered and (*F*) membrane-tethered states. (*Insets*) Refined tether structures (see also Fig. S4). Fitting a molecular model of the ground state proteasome (26) into the EM density maps shows that both extra densities bind at Rpn9 (light green).

By mapping the different proteasome classes back into the cellular volumes (Fig. S6 and Movie S1), we were able to compare the assembly states, functional states, and binding states of cytoplasmic and nuclear proteasomes. We found that the ratios of single-capped to double-capped and ground state to substrate-processing state were nearly identical between nuclear and cytoplasmic proteasomes (Fig. 2*D*). Furthermore, the ratio of functional states remained relatively constant for all 19S particles, independent of assembly state or binding state (Fig. S5). This level of functional activity was similar to the level previously reported for cytoplasmic proteasomes in rat neurons (i.e., 20% substrate-processing state) (23) and thus, may represent an evolutionarily conserved baseline for proteasome activity in unstressed cells. In contrast to the evenly distributed assembly and functional states, all of the basket-tethered and membrane-tethered binding states were localized to the nucleus, where they comprised 43% of the nuclear proteasome population (Fig. 2*D*). Whereas the free binding state class was dispersed throughout the nucleoplasm, the basket-tethered and membrane-tethered proteasomes were exclusively found at the INM, close to NPCs (Fig. S7 *A* and *C*). Intriguingly, the two distinct peaks of proteasome concentration that we had observed adjacent to the INM (Fig. 1*F*) were each composed of a different class of tethered proteasomes (Fig. S7*A*). Thus, these two classes of tethered proteasomes, which were identified solely by image-based classification and not positional information, have distinct spatial distributions within the cell.

To explore the spatial relationships between tethered proteasomes and NPCs, we generated an in situ average of the NPCs in our tomograms (Fig. S8), which we refined by individually aligning asymmetric substructures to compensate for the pore's flexibility, as previously described (31). Plotting the positions of Rpn9, which marks the tether attachment site, for every basket-tethered and membrane-tethered 19S particle relative to the NPC center and the INM showed that these binding state classes are two completely separate populations, with no positional overlap (Fig. 3*A*). While the membrane-tethered class is anchored at the INM, the basket-tethered class is localized to a region that is occupied by the NPC nuclear basket, a flexible filamentous structure that extends ∼40–80 nm from the INM into the nucleoplasm (14, 32–34).

We plotted the Rpn9 positions radially relative to the closest NPC asymmetric unit, and then symmetrized these heat maps according to the eightfold symmetry of the NPC for clearer visualization (Fig. 3*B*). The basket-tethered positions overlaid the NPC with eight sharp peaks, suggesting that the basket serves as a scaffold with one binding site at each NPC asymmetric unit. In contrast, the membrane-tethered positions formed a well-delineated circle around the NPC periphery, with at least two peaks per NPC asymmetric unit. Thus, the membrane-tethered class may have more available binding sites at the NPC than the basket-tethered class. We hypothesize that the increased binding capacity for membrane-tethered proteasomes may be related to the multiple membrane protrusions that we observed in the focused subtomogram alignment of the tethering region (Fig. 2*F* and Fig. S4*B*). Interestingly, the yeast INM protein Cut8 is proposed to dimerize and anchor two proteasomes to the INM through ubiquitin tethers (11). Such a dimerized tethering protein could provide an increased number of binding sites for the membrane-tethered proteasomes at the NPC.

Both the regular spacing of basket-tethered proteasomes and the high occupancy of membrane-tethered proteasomes could be clearly observed at individual NPCs in our tomograms (Fig. 3*C* and Movie S2). The proteasomes of both classes aligned their long axes toward the NPC center (Fig. S7*D*), with their tethered caps facing the NPC. Each class also had a specific inclination relative to the membrane (Fig. S7*B*). Of the NPCs with >75% of their structures contained within the tomogram volumes, 40% were associated with basket-tethered proteasomes (with 3.3 ± 1.7 per NPC), 87% were associated with membrane-tethered proteasomes (with 4.5 ± 2.6 per NPC), 39% were associated with both, and only 12% were associated with neither.

The NPC basket is constructed from thin TPR filaments that are too flexible to be resolved in structural averages of the NPC (31, 35). However, in some high-quality tomograms, we were able to visualize individual basket filaments projecting from the NPC into the nucleoplasm (Fig. 4 *A*–*I*). These filaments were uniformly spaced around the NPC and connected the basket-tethered

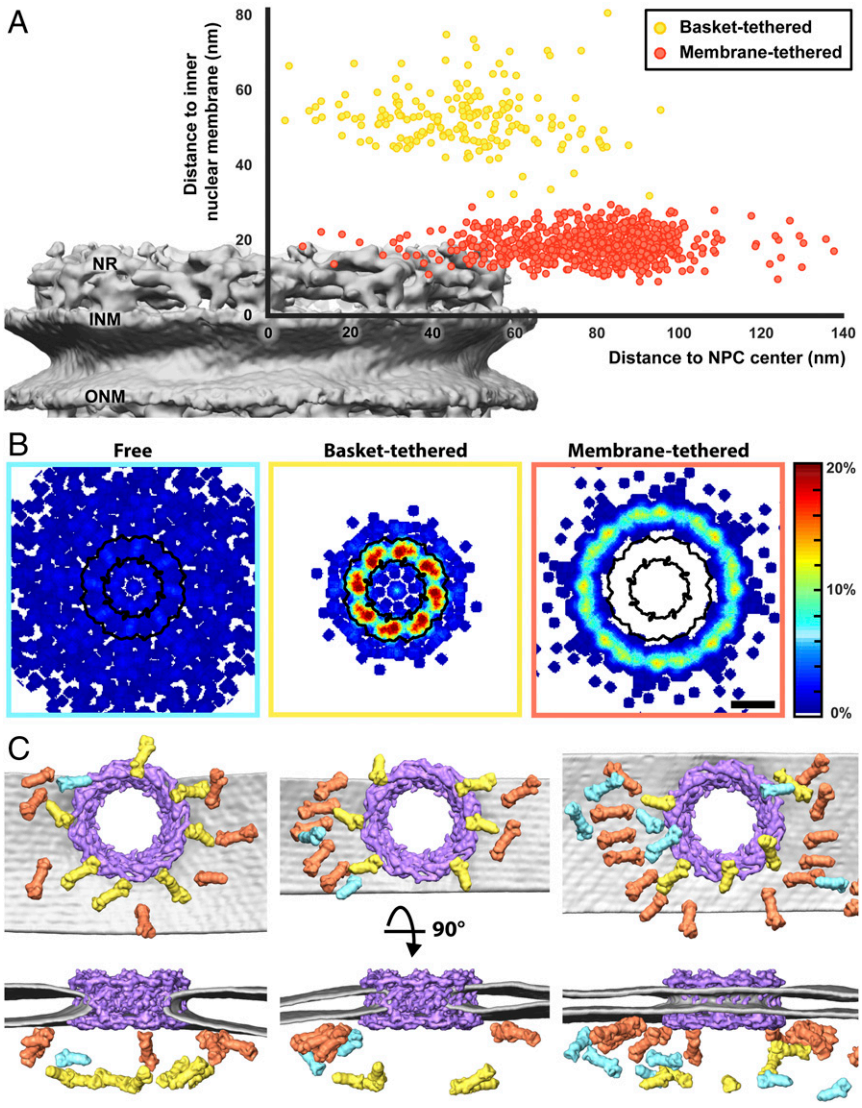

Fig. 3. Proteasomes bind two distinct sites at NPCs. (*A*) Proteasome Rpn9 positions relative to the NPC center and INM. There is no positional overlap between basket-tethered and membrane-tethered classes. All proteasomes in the dataset were plotted. Uncertainty in estimating the NPC center position for incomplete NPCs resulted in dispersion of proteasome positions along the *x* axis. NR, nuclear ring; ONM, outer nuclear membrane. (*B*) Heatmaps for each binding state, showing proteasome Rpn9 positions symmetrized around the NPC (black silhouette). Orthographic views facing the NPC from the nucleus. Heatmaps were normalized by the number of proteasomes in each class. Only proteasomes adjacent to NPCs with >75% of their structures contained within the tomogram were plotted, resulting in more precise localization. Double-capped proteasomes were plotted only once, using the tethered cap if applicable. (Scale bar: 50 nm.) (*C*) Close-up orthographic views of structures mapped into three different tomograms, showing NPCs (purple) surrounded by free (blue), basket-tethered (yellow), and membrane-tethered (orange) proteasomes. (*Top* row) Views from the nucleus; (*Bottom* row) views along the nuclear envelope (gray).

proteasomes to the NPC's nuclear ring. In search of additional structural evidence for the binding interaction between proteasomes and the NPC basket, we mapped the focused subtomogram alignment of the basket-tethered class (Fig. 2*E* and Fig. S4*A*) into the cellular volumes. Compellingly, the bifurcated extra densities tethered to these proteasomes aligned with each other to reconstitute the flexible round shape of the basket (Fig. 4 *J* and *K*); based on their collective shape and distance from the NPC, the extra densities are likely part of the basket's distal ring. Thus, we conclude that this class of proteasomes is tethered to the NPC basket. Using basket-tethered proteasomes as fiducial markers for the NPC basket, we were able to measure the flexibility of the native basket structure within the cellular environment (Fig. 4 *J* and *K*). The basket is subject to distortions in its elliptical shape (Fig. 4*K*, green ring) as well as translational shifts to its center position relative to the NPC (Fig. 4*K*, blue ring).

Discussion

The two classes of NPC-localized proteasomes likely perform nonredundant functions. The basket-tethered class is optimally positioned to encounter soluble proteins transiting the NPC's central channel. Similarly, the membrane-tethered proteasomes are in an ideal location to encounter membrane proteins traveling through the NPC's peripheral channels. Therefore, one plausible function for both classes is the surveillance of NPC traffic (Fig. 5). The INM is continuous with the outer nuclear membrane (ONM) and endoplasmic reticulum (ER), and membrane proteins with sufficiently small extraluminal domains can freely diffuse across the NPC (36). Thus, the INM requires a quality control mechanism to maintain its distinct identity. In *S. cerevisiae*, the Asi E3 ubiquitin ligase mediates a specialized branch of ER-associated degradation (ERAD), destroying mislocalized membrane proteins that reach the INM (37, 38). The membrane-tethered proteasomes may participate in this specialized ERAD, encircling the NPCs to form an INM quality control checkpoint.

The high proteasome concentration at NPCs might additionally enable this region to function as a degradation center where unneeded proteins are sent for recycling (Fig. 5). Existing nuclear import and export signals could be coopted to target substrates to the NPC-tethered proteasomes. While the targeting of nuclear proteins seems more practical as it does not require passage through the NPC, numerous proteins have also been shown to undergo nuclear import for degradation (1, 39, 40). The NPC-tethered proteasomes may also degrade kinetochore components, as the localization of proteasomes to the nuclear envelope is required for maintaining correct kinetochore stoichiometry in *S. pombe* (13). In addition, some regions of transcriptionally active chromatin physically interact with the NPC's nuclear basket (14, 41), so basket-tethered

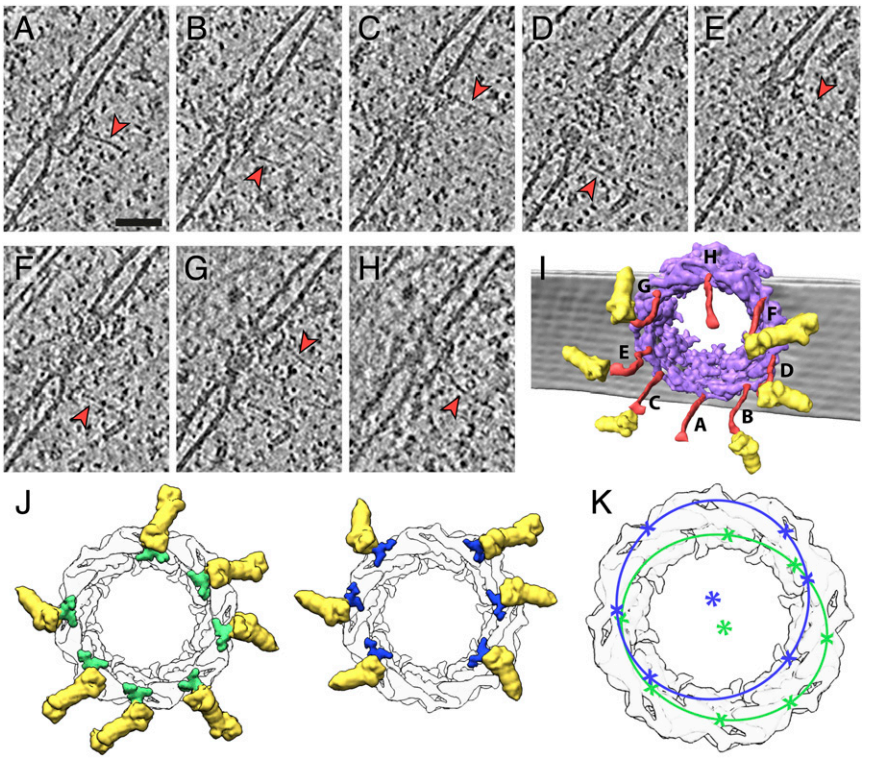

Fig. 4. Proteasomes tether to the NPC nuclear basket. (*A–H*) Sequential slices through a tomographic volume of an NPC (from Fig. 1*A*, rotated 180°). Thin filaments (red arrows) extend from the NPC into the nucleoplasm. Some filaments are straight, while others are slightly curved. The filament in *E* appears to be buckled. Attachment of the filaments to basket-tethered proteasomes is visible in slices *B*, *D*, and *F*. In *C* and *G*, the attached proteasome is out of the plane of the slice. (Scale bar: 50 nm.) (*I*) Segmentation of the filaments (red) from *A–H* shows that they connect the basket-tethered proteasomes (yellow) to the NPC (purple). Perspective view from the nucleus. (*J*) NPCs (white) mapped into tomograms along with hybrid structures of basket-tethered proteasomes (yellow) fused with the focused alignment of this class's extra density (green and blue). The extra densities align in a round shape. Orthographic views from the nucleus. (*K*) For both examples in *J*, the positions of tethered Rpn9 (X) were fit with an ellipse, reconstituting the shape of the flexible NPC basket. Asterisks indicate ellipse geometrical centers.

proteasomes are well positioned to modulate gene expression by degrading transcription factors (2, 42) and perhaps by regulating chromatin remodeling (43). Lastly, the NPC may serve as a staging site for proteasome export to the cytoplasm during stress conditions or quiescence (3, 44).

It remains an open question how the proteasomes are recruited to NPCs. Proteasome structures with extra densities are only found close to NPCs (Figs. S6 and S7*C*). Thus, the tethering proteins likely do not escort proteasomes to the NPC, but rather are resident at the NPC and bind proteasomes that come near, perhaps by capturing proteasomes completing nuclear import. Although there are two distinct tethering sites at NPCs (Fig. 3 *A* and *B*), both basket-tethered and membrane-tethered proteasomes are bound at their Rpn9 subunit (Fig. 2 *E* and *F*). Therefore, either one protein mediates proteasome tethering to two different NPC sites or there are two different tethering proteins that can both bind Rpn9.

Our observations in algae raise questions about the evolutionary conservation of NPC-tethered proteasomes. While yeast may indeed employ a similar mechanism, the proteins likely differ; Cut8/Sts1 (10–12), Esc1 (14), and the Asi complex (37, 38) have no obvious homologs in *Chlamydomonas*. Cut8 is believed to bind the Rpn11 proteasome subunit (45), whereas we resolve binding of the tethering densities at Rpn9 (Fig. 2 *E* and *F* and Fig. S4). Immunoprecipitation experiments indicate that Esc1 only transiently interacts with the NPC basket but strongly interacts with proteasomes, suggesting that Esc1 may also be bound to free proteasomes (14). In contrast, the high occupancy of proteasomes that we observed at specific NPC sites implies a less transient tethering interaction, and no extra density was found attached to free proteasomes (Fig. 2*C*). Although in situ identification of macromolecules is more difficult in yeast due to a crowded cellular environment, it will be interesting to examine how the localization of Cut8- and Esc1-bound proteasomes compare with the NPC-tethered proteasomes that we characterized in this study. As for *Chlamydomonas*, the next important step will be to identify the tethering proteins bound to Rpn9 using the wealth of genetic and molecular tools available in this model organism (46).

The conservation of NPC-tethered proteasomes in metazoans is even less clear. While a Cut8-like protein has been shown to recruit proteasomes to the nuclear envelope of *Drosophila* S2 cells (10), there do not appear to be abundant proteasomes at the nuclear envelope or NPCs of HeLa cells (47). Unlike metazoans, *Chlamydomonas* and yeast both undergo a closed mitosis (48). Without mitotic breakdown of the nuclear envelope, their only opportunity to target proteins to the INM is through the NPC (36). A closed mitosis would also favor nuclear accumulation of undesirable soluble proteins over multiple generations. Thus, surveillance of NPC traffic and quality control of the INM may be

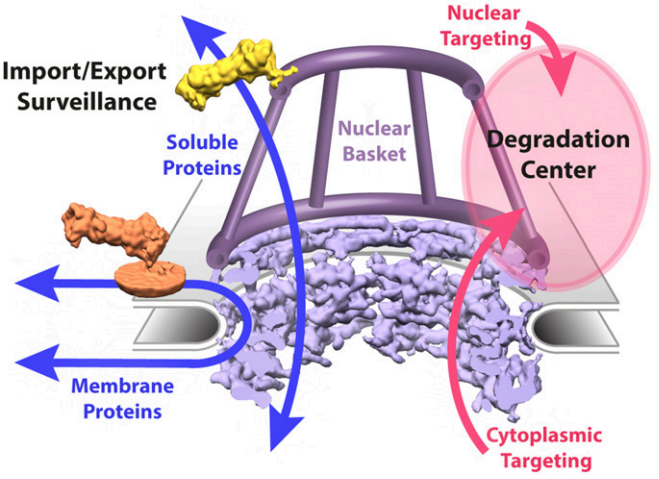

Fig. 5. Proposed quality control functions for proteasomes at the NPC. Basket-tethered and membrane-tethered proteasomes may perform surveillance of transiting soluble and membrane proteins, respectively (blue). The abundant NPC-tethered proteasomes could also serve as a degradation center where nuclear and cytoplasmic proteins are sent for destruction (pink). This degradation center may also function in transcriptional control.

more important for cells that cannot refresh the contents of their nuclei during cell division. Following this logic, it will be interesting to observe the distribution of nuclear proteasomes in terminally differentiated mammalian cells.

Materials and Methods

A detailed description of cryo-FIB, cryo-ET, and image analysis is found in *SI Materials and Methods*.

ACKNOWLEDGMENTS. We thank S. Pfeffer, R. Engelmeier, and D. Tegunov for assistance with Fig. 1; K. Engel for critical reading; and F. Förster, C. Lee, T. Schaffer, E. Sakata, and R. Fernandez-Busnadiego for helpful discussions. This work was supported by the European Molecular Biology Laboratory (EMBL) Interdisciplinary Postdoctoral Program under Marie Curie COFUND Actions (S.M.); European Research Council Grant 309271-NPCAtlas (to M.B.); the Deutsche Forschungsgemeinschaft Excellence Cluster Center for Integrated Protein Science Munich, SFB-1035/Project A01 (to W.B.); EMBL; and the Max Planck Society.

1. Gallagher PS, Oeser ML, Abraham AC, Kaganovich D, Gardner RG (2014) Cellular maintenance of nuclear protein homeostasis. *Cell Mol Life Sci* 71:1865–1879.
2. Durairaj G, Kaiser P (2014) The 26S proteasome and initiation of gene transcription. *Biomolecules* 4:827–847.
3. Enenkel C (2014) Proteasome dynamics. *Biochim Biophys Acta* 1843:39–46.
4. Pack CG, et al. (2014) Quantitative live-cell imaging reveals spatio-temporal dynamics and cytoplasmic assembly of the 26S proteasome. *Nat Commun* 5:3396.
5. Gardner RG, Nelson ZW, Gottschling DE (2005) Degradation-mediated protein quality control in the nucleus. *Cell* 120:803–815.
6. Dang FW, Chen L, Madura K (2016) Catalytically active proteasomes function predominantly in the cytosol. *J Biol Chem* 291:18765–18777.
7. Chen L, Madura K (2014) Yeast importin-α (Srp1) performs distinct roles in the import of nuclear proteins and in targeting proteasomes to the nucleus. *J Biol Chem* 289: 32339–32352.
8. Wójcik C, DeMartino GN (2003) Intracellular localization of proteasomes. *Int J Biochem Cell Biol* 35:579–589.
9. Fabunmi RP, Wigley WC, Thomas PJ, DeMartino GN (2001) Interferon gamma regulates accumulation of the proteasome activator PA28 and immunoproteasomes at nuclear PML bodies. *J Cell Sci* 114:29–36.
10. Takeda K, Yanagida M (2005) Regulation of nuclear proteasome by Rhp6/Ubc2 through ubiquitination and destruction of the sensor and anchor Cut8. *Cell* 122: 393–405.
11. Takeda K, et al. (2011) Implications for proteasome nuclear localization revealed by the structure of the nuclear proteasome tether protein Cut8. *Proc Natl Acad Sci USA* 108:16950–16955.
12. Chen L, et al. (2011) Sts1 plays a key role in targeting proteasomes to the nucleus. *J Biol Chem* 286:3104–3118.
13. Salas-Pino S, Gallardo P, Barrales RR, Braun S, Daga RR (2017) The fission yeast nucleoporin Alm1 is required for proteasomal degradation of kinetochore components. *J Cell Biol* 216:3591–3608.
14. Niepel M, et al. (2013) The nuclear basket proteins Mlp1p and Mlp2p are part of a dynamic interactome including Esc1p and the proteasome. *Mol Biol Cell* 24: 3920–3938.
15. Asano S, Engel BD, Baumeister W (2016) In situ cryo-electron tomography: A post-reductionist approach to structural biology. *J Mol Biol* 428:332–343.
16. Schaffer M, et al. (2017) Optimized cryo-focused ion beam sample preparation aimed at in situ structural studies of membrane proteins. *J Struct Biol* 197:73–82.
17. Marko M, Hsieh C, Schalek R, Frank J, Mannella C (2007) Focused-ion-beam thinning of frozen-hydrated biological specimens for cryo-electron microscopy. *Nat Methods* 4: 215–217.
18. Rigort A, et al. (2012) Focused ion beam micromachining of eukaryotic cells for cryoelectron tomography. *Proc Natl Acad Sci USA* 109:4449–4454.
19. Engel BD, et al. (2015) In situ structural analysis of Golgi intracisternal protein arrays. *Proc Natl Acad Sci USA* 112:11264–11269.
20. Pfeffer S, et al. (2017) Dissecting the molecular organization of the translocon-associated protein complex. *Nat Commun* 8:14516.
21. Freeman Rosenzweig ES, et al. (2017) The eukaryotic CO_2-concentrating organelle is liquid-like and exhibits dynamic reorganization. *Cell* 171:148–162.
22. Bykov YS, et al. (2017) The structure of the COPI coat determined within the cell. *eLife* 6:e32493.
23. Asano S, et al. (2015) Proteasomes. A molecular census of 26S proteasomes in intact neurons. *Science* 347:439–442.
24. Enenkel C, Lehmann A, Kloetzel PM (1998) Subcellular distribution of proteasomes implicates a major location of protein degradation in the nuclear envelope-ER network in yeast. *EMBO J* 17:6144–6154.
25. Wilkinson CRM, et al. (1998) Localization of the 26S proteasome during mitosis and meiosis in fission yeast. *EMBO J* 17:6465–6476.
26. Unverdorben P, et al. (2014) Deep classification of a large cryo-EM dataset defines the conformational landscape of the 26S proteasome. *Proc Natl Acad Sci USA* 111: 5544–5549.
27. Wehmer M, et al. (2017) Structural insights into the functional cycle of the ATPase module of the 26S proteasome. *Proc Natl Acad Sci USA* 114:1305–1310.
28. Takeuchi J, Fujimuro M, Yokosawa H, Tanaka K, Toh-e A (1999) Rpn9 is required for efficient assembly of the yeast 26S proteasome. *Mol Cell Biol* 19:6575–6584.
29. Riedinger C, et al. (2010) Structure of Rpn10 and its interactions with polyubiquitin chains and the proteasome subunit Rpn12. *J Biol Chem* 285:33992–34003.
30. Sakata E, et al. (2012) Localization of the proteasomal ubiquitin receptors Rpn10 and Rpn13 by electron cryomicroscopy. *Proc Natl Acad Sci USA* 109:1479–1484.
31. von Appen A, et al. (2015) In situ structural analysis of the human nuclear pore complex. *Nature* 526:140–143.
32. Krull S, Thyberg J, Björkroth B, Rackwitz HR, Cordes VC (2004) Nucleoporins as components of the nuclear pore complex core structure and Tpr as the architectural element of the nuclear basket. *Mol Biol Cell* 15:4261–4277.
33. Frosst P, Guan T, Subauste C, Hahn K, Gerace L (2002) Tpr is localized within the nuclear basket of the pore complex and has a role in nuclear protein export. *J Cell Biol* 156:617–630.
34. Jarnik M, Aebi U (1991) Toward a more complete 3-D structure of the nuclear pore complex. *J Struct Biol* 107:291–308.
35. Eibauer M, et al. (2015) Structure and gating of the nuclear pore complex. *Nat Commun* 6:7532.
36. Katta SS, Smoyer CJ, Jaspersen SL (2014) Destination: Inner nuclear membrane. *Trends Cell Biol* 24:221–229.
37. Foresti O, Rodriguez-Vaello V, Funaya C, Carvalho P (2014) Quality control of inner nuclear membrane proteins by the Asi complex. *Science* 346:751–755.
38. Khmelinskii A, et al. (2014) Protein quality control at the inner nuclear membrane. *Nature* 516:410–413.
39. Prasad R, Kawaguchi S, Ng DTW (2010) A nucleus-based quality control mechanism for cytosolic proteins. *Mol Biol Cell* 21:2117–2127.
40. Park SH, et al. (2013) PolyQ proteins interfere with nuclear degradation of cytosolic proteins by sequestering the Sis1p chaperone. *Cell* 154:134–145.
41. Ibarra A, Hetzer MW (2015) Nuclear pore proteins and the control of genome functions. *Genes Dev* 29:337–349.
42. Skelly MJ, Frungillo L, Spoel SH (2016) Transcriptional regulation by complex interplay between post-translational modifications. *Curr Opin Plant Biol* 33:126–132.
43. McCann TS, Tansey WP (2014) Functions of the proteasome on chromatin. *Biomolecules* 4:1026–1044.
44. Laporte D, Salin B, Daignan-Fornier B, Sagot I (2008) Reversible cytoplasmic localization of the proteasome in quiescent yeast cells. *J Cell Biol* 181:737–745.
45. Tabb MM, Tongaonkar P, Vu L, Nomura M (2000) Evidence for separable functions of Srp1p, the yeast homolog of importin alpha (karyopherin alpha): Role for Srp1p and Sts1p in protein degradation. *Mol Cell Biol* 20:6062–6073.
46. Jinkerson RE, Jonikas MC (2015) Molecular techniques to interrogate and edit the Chlamydomonas nuclear genome. *Plant J* 82:393–412.
47. Mahamid J, et al. (2016) Visualizing the molecular sociology at the HeLa cell nuclear periphery. *Science* 351:969–972.
48. Cross FR, Umen JG (2015) The Chlamydomonas cell cycle. *Plant J* 82:370–392.
49. Umen JG, Goodenough UW (2001) Control of cell division by a retinoblastoma protein homolog in Chlamydomonas. *Genes Dev* 15:1652–1661.
50. Schaffer M, et al. (2015) Cryo-focused ion beam sample preparation for imaging vitreous cells by cryo-electron tomography. *Bio Protoc* 5:e1575.
51. Mastronarde DN (2005) Automated electron microscope tomography using robust prediction of specimen movements. *J Struct Biol* 152:36–51.
52. Zheng SQ, et al. (2017) MotionCor2: Anisotropic correction of beam-induced motion for improved cryo-electron microscopy. *Nat Methods* 14:331–332.
53. Kremer JR, Mastronarde DN, McIntosh JR (1996) Computer visualization of three-dimensional image data using IMOD. *J Struct Biol* 116:71–76.
54. Frangakis AS, et al. (2002) Identification of macromolecular complexes in cryoelectron tomograms of phantom cells. *Proc Natl Acad Sci USA* 99:14153–14158.
55. Hrabe T, et al. (2012) PyTom: A python-based toolbox for localization of macromolecules in cryo-electron tomograms and subtomogram analysis. *J Struct Biol* 178: 177–188.
56. Chen Y, Pfeffer S, Hrabe T, Schuller JM, Förster F (2013) Fast and accurate reference-free alignment of subtomograms. *J Struct Biol* 182:235–245.
57. Bharat TA, Russo CJ, Löwe J, Passmore LA, Scheres SH (2015) Advances in single-particle electron cryomicroscopy structure determination applied to sub-tomogram averaging. *Structure* 23:1743–1753.
58. Rohou A, Grigorieff N (2015) CTFFIND4: Fast and accurate defocus estimation from electron micrographs. *J Struct Biol* 192:216–221.
59. Chen Y, Pfeffer S, Fernández JJ, Sorzano CO, Förster F (2014) Autofocused 3D classification of cryoelectron subtomograms. *Structure* 22:1528–1537.
60. Goddard TD, Huang CC, Ferrin TE (2007) Visualizing density maps with UCSF Chimera. *J Struct Biol* 157:281–287.
61. Beck M, Lučić V, Förster F, Baumeister W, Medalia O (2007) Snapshots of nuclear pore complexes in action captured by cryo-electron tomography. *Nature* 449:611–615.
62. Bui KH, et al. (2013) Integrated structural analysis of the human nuclear pore complex scaffold. *Cell* 155:1233–1243.
63. Scheres SHW (2012) RELION: Implementation of a Bayesian approach to cryo-EM structure determination. *J Struct Biol* 180:519–530.